NANO · MICRO small
www.small-journal.com

Design and Realization of 3D Printed AFM Probes

*Nourin Alsharif, Anna Burkatovsky, Charles Lissandrello, Keith M. Jones, Alice E. White, and Keith A. Brown**

Atomic force microscope (AFM) probes and AFM imaging by extension are the product of exceptionally refined silicon micromachining, but are also restricted by the limitations of these fabrication techniques. Here, the nanoscale additive manufacturing technique direct laser writing is explored as a method to print monolithic cantilevered probes for AFM. Not only are 3D printed probes found to function effectively for AFM, but they also confer several advantages, most notably the ability to image in intermittent contact mode with a bandwidth approximately ten times larger than analogous silicon probes. In addition, the arbitrary structural control afforded by 3D printing is found to enable programming the modal structure of the probe, a capability that can be useful in the context of resonantly amplifying nonlinear tip–sample interactions. Collectively, these results show that 3D printed probes complement those produced using conventional silicon micromachining and open the door to new imaging techniques.

Advances in silicon micromachining have fueled decades of advances in microelectromechanical systems (MEMS) that have impacted nearly every area of science and technology.[1] One example that is particularly relevant to nanoscience, atomic force microscopy (AFM) comprises a suite of techniques for interrogating and patterning nanoscale materials and is based upon the use of microscopic cantilevers that are machined using techniques drawn from conventional silicon micromachining.[2] The fabrication of AFM probes is an especially illustrative example of the opportunities and limitations of conventional micromachining in that it traditionally consists of a series of lithographic steps that define 2D patterns followed by processing steps that add or remove material using the 2D pattern as a mask. Through cleverly designing these procedures, limited 3D designs can be realized, namely the sharp-tipped suspended probes that enable AFM.[3] However, the structures that can be realized using this approach are intrinsically limited both in the materials available and the complexity of the resultant structures, especially in the third dimension. In contrast with this layer-by-layer approach, additive manufacturing is a different paradigm of machining wherein material is selectively added to define fully 3D structures with significantly more freedom.[4] Of the myriad additive manufacturing approaches that have been explored, direct laser writing (DLW) lithography using two photon polymerization is of particular interest as it allows one to write 3D structures in a single process with resolution that, in some cases, surpasses the single photon diffraction limit.[5] As such, this approach has been useful for studying diverse phenomena from mechanics to biomedicine.[6] Recently, DLW lithography was applied as a method for post-processing conventional silicon AFM probes to tailor their resonant properties.[7] However, the question remains as to whether DLW lithography can itself be used to construct entire AFM probes and whether such probes would confer any advantages.

Here, we explore how 3D printing can transform AFM by realizing new and unique probe designs (**Figure 1**). To begin, we explore a general process for printing monolithic probes with DLW lithography and mounting them in an AFM, thus overcoming the challenge of bridging the microscopic length scales that can be addressed by DLW lithography and the much larger length scales that need to be controlled in order to handle probe chips macroscopically. Following this, we characterize the 3D printed probes using a commercial AFM system and find that cantilever structures provide a useful way of exploring how material properties are affected by printing conditions. Importantly, not only were these probes capable of imaging topographical features in both contact mode and intermittent contact mode, but the low quality factor of polymer probes drastically increased the bandwidth of these probes relative to their silicon counterparts and enabled high speed scanning. Having shown that simple 3D printed probes can be used for AFM, we sought to make inroads into the vast landscape of structures that can be realized with 3D printing to learn what new imaging capabilities can be garnered by the design, fabrication, and testing of more complex geometries. In particular, we explored bisegmented probes that allowed us to independently tune the first and second vibrational resonance frequencies. Taken together, these results show that 3D printed polymer probes can be used

N. Alsharif, A. Burkatovsky, Dr. C. Lissandrello,
Prof. A. E. White, Prof. K. A. Brown
Department of Mechanical Engineering
Boston University
110 Cummington Mall, Boston, MA 02215, USA
E-mail: brownka@bu.edu
K. M. Jones
Oxford Instruments Asylum Research, Inc.
6310 Hollister Avenue, Santa Barbara, CA 93117, USA
Prof. A. E. White, Prof. K. A. Brown
Physics Department and Division of Materials Science and Engineering
590 Commonwealth Avenue, Boston, MA 02215, USA
The ORCID identification number(s) for the author(s) of this article can be found under https://doi.org/10.1002/smll.201800162.

DOI: 10.1002/smll.201800162

for AFM and that the arbitrary structural control afforded by 3D printing provides new possibilities for AFM imaging. More generally, this work provides an example of how additive manufacturing can augment conventional silicon micromachining to enable new scientific and technological opportunities.

In order to study the potential for 3D printed components to perform as AFM probes, it is necessary to bridge a major gap in length scales. Specifically, the probe of an AFM is a microscopic object composed of a 100 µm scale cantilever and a conical tip that comes to a nanoscopic point. The sharp tip interacts with the sample enabling nanoscale imaging while the cantilever acts as a mechanical spring and serves as a reflector for a laser spot. While this cantilevered probe is responsible for both interacting with the sample and reporting the observed force, it comprises a miniscule fraction of the total mass of the millimeter-scale chip to which the probe is typically attached. The macroscopic size of the chip enables one to readily manipulate it using tweezers and position it inside an AFM. In the case of AFM probes made using conventional silicon micromachining, both the probe and chip are machined out of the same wafer. However, this monolithic approach is not suitable for 3D printing; the large mismatch in size scale between the probe and the chip poses a problem for DLW, which has the resolution to fabricate complex cantilever geometries but lacks the throughput to effectively fabricate the macroscopic chip.

As a means of minimizing the material to be printed while ensuring compatibility with commercial AFM systems, we developed a transfer-based method for constructing 3D printed AFM probes. In a typical experiment, an array of probes with corresponding supporting blocks were designed and printed out of a photosensitive polymer (IP-dip—Nanoscribe GmbH) using a dip-in lithography mode (Figure 1). This process was carried out using a commercial DLW system (Nanoscribe Photonic Professional GT). The focal spot of a 780 nm laser is raster scanned through a liquid droplet of uncrosslinked polymer by high speed galvo scanners (>40 mm s^{-1}), crosslinking a desired structure through two photon absorption. After DLW, the remaining uncrosslinked polymer is rinsed away. The minimum feature size in the plane perpendicular to the beam is 200 nm when using a 25× objective and 100 nm when using a 63× objective.

Surface roughness is a key characteristic of AFM probes as it can limit specular reflection and thus hinder the sensitivity of the optical lever used for AFM feedback. Here, printing parameters such as slicing (distance between subsequent layers printed) and hatching (distance between scan lines on the layers parallel to the substrate) were optimized with respect to the voxel geometry to maximum overlap and minimize surface roughness (**Figure 2**a and Figure S1a,b, Supporting Information). For example, when printing with a 25× objective (voxel width 500 nm and height 6–7 µm), we were only able to obtain workable probes with slicing and hatching values of 200 nm. We quantified the roughness using tapping mode AFM and found the printed polymers to have a 5.6 nm root mean squared roughness, consistent with literature reports.[8] In addition, both the supporting block and probes were printed pointing out of the substrate plane (Figure S1c, Supporting Information), which alleviates undesirable complications of DLW of cantilevered structures such as stiction.

The supporting blocks were small enough to enable rapid printing (<10 min print time for a block supporting three probes, printed with low resolution) but large enough to manually manipulate after printing. The blocks were typically 500 µm wide, 200 µm thick, and ≈300 µm high, while the printed probes have dimensions commensurate with typical AFM probes. With regard to the placement of multiple probes on the support block, it is important that each probe be separated from its neighboring probe by a distance of more than three times the probe width as simulation (COMSOL Multiphysics) predicts that the principle vibrational modes of the probes will otherwise become coupled through the supporting block (Figure S1c,d, Supporting Information). Once printed, the supporting block was detached from the printing substrate (typically a silicon chip) with tweezers and manually adhered to a probe-less AFM chip using an acrylate epoxy.

As a final processing step, the nearly transparent polymer probes were rendered reflective by coating both their front and back sides with 28 nm of aluminum using an electron beam evaporator (EVOVAC—Angstrom). Aluminum was chosen as a reflective coating due to its low melting temperature and low density compared to other metals. The 28 nm coating thickness was selected as a compromise between reflectivity and probe mechanics. Thicker coatings (>50 nm) can improve optical lever performance but often cause irreversible bending in the probe during deposition due to the mismatch in the coefficients of thermal expansion. The mechanical properties of aluminum are strongly influenced by a thin oxide that forms in atmospheric conditions, the presence of which must be included when considering the mechanics of aluminum films. It is important to emphasize that, after this step is complete, the final structure is compatible with commercial AFM systems (seen in Figure 1d with an Oxford Instruments MFP-3D AFM).

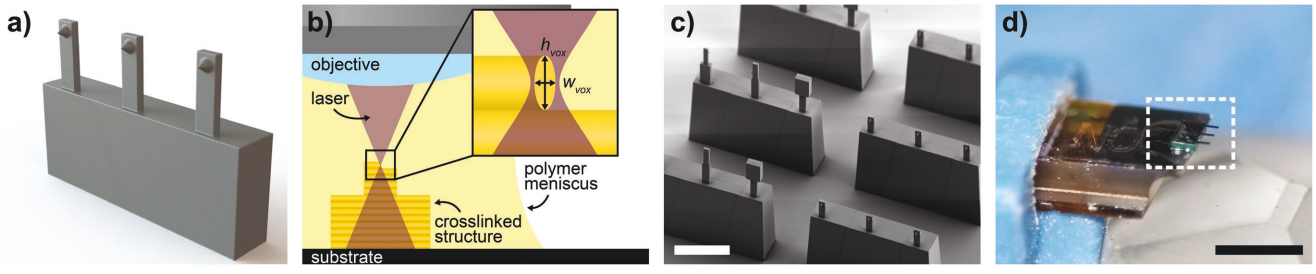

Figure 1. a) Design of three probes attached to a support block. b) Schematic of the 3D printing system showing a partially printed structure within a meniscus of uncrosslinked polymer. The inset at the focal plane of the laser shows the high aspect ratio voxel with height h_{vox} and width w_{vox}. c) Scanning electron microscope (SEM) image showing a variety of 3D printed probes written during one session. Scale bar is 200 µm. d) Optical microscope image of three aluminum coated probes adhered to an AFM chip, a white box outlines both the supporting block and the probes. Scale bar is 1 mm.

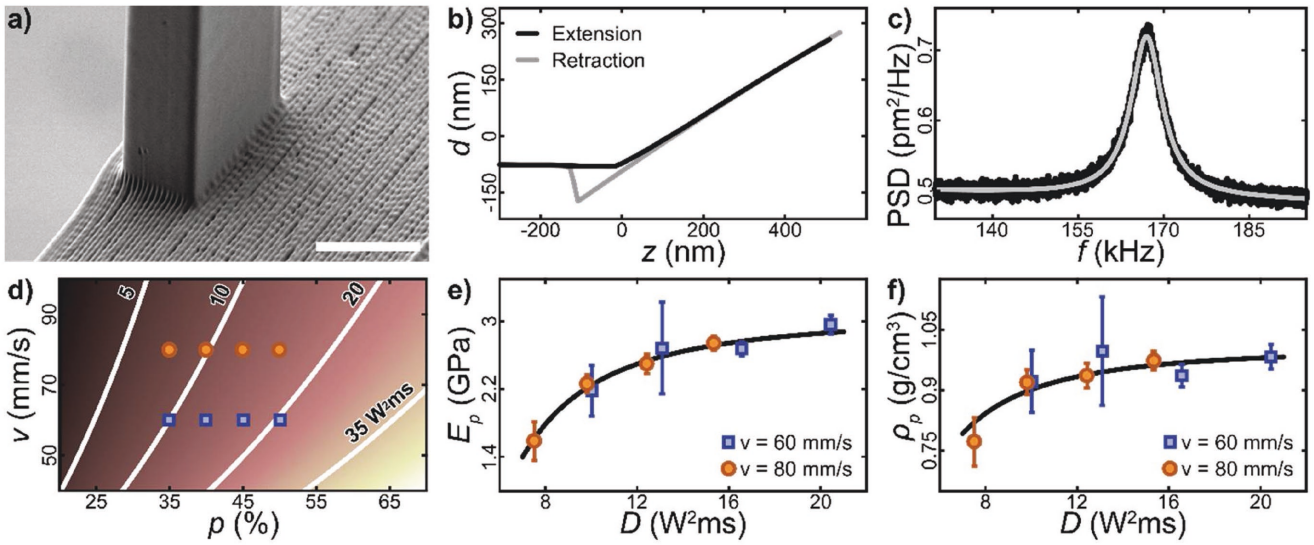

Figure 2. a) SEM image showing the intersection of a 3D printed probe and support block. To improve optical lever performance, the probe was printed with 200 nm resolution while the support block was printed with 1.5 µm resolution. Scale bar is 15 µm. b) Atomic force microscope (AFM) measured deflection d of a printed probe in contact with a stiff substrate versus its vertical position z, the positively sloped portion provides a calibration of optical lever sensitivity. c) AFM measured power spectral density (PSD) versus frequency f of a printed probe in the region of its first vibrational resonance, with Lorentzian fit (principle harmonic resonance frequency f_p = 167 kHz, quality factor Q = 29.1). d) Map of delivered dose D versus writing power p and scan speed v, with specified contours of constant D. Points indicate specific combinations shown in (e) and (f). e) Calculated elastic modulus E_p of printed probes versus D. f) Density of polymer ρ_p versus D. Solid lines in (e) and (f) represent fits as described in the text.

Having printed and mounted probes, we sought to explore the ability of these probes to operate in an AFM system. As with all AFM probes, it is necessary to characterize the properties of the probe before performing imaging experiments. Specifically, probes can be parametrized by either their geometric parameters and material properties such as elastic modulus E and density ρ or as a lumped element spring-mass-dashpot system that is defined by a spring constant k, resonant frequency f_p, and quality factor Q. In a typical AFM context, users are generally only concerned with the latter parametrization as these parameters can be easily extracted using standard AFM procedures. Thus, we began characterizing 3D printed probes by studying their lumped element parameters using standard AFM techniques. In brief, a probe of interest was mounted in an AFM system, aligned for optical readout, and carefully lowered until it made contact with a rigid surface. This process allows one to compute the optical lever sensitivity, which represents a conversion between the voltage registered by the photodiode in the optical lever system and the deflection of the probe (Figure 2b). After the probe was raised out of contact from the surface, the thermal motion of the probe was observed to generate a power spectrum of motion which can be directly fit to extract both the resonance frequency of the principle harmonic f_p and corresponding quality factor Q (Figure 2c). Additionally, the area under the peak is used to compute the spring constant k by leveraging equipartition.[9] In experiments that were used to evaluate the properties of the probes, the probes were cantilevered beams printed without tips. For a typical experiment on a probe that is designed to be 170 µm long, 35 µm wide, and 10 µm thick, printed with slicing and hatching distances of 200 nm, scan speed v of 80 mm s^{-1}, and laser power p of 45%, we found k = 9.11 ± 0.23 N m^{-1}, Q = 28.9 ± 0.5, and f_p = 124.23 ± 0.91 kHz.

In order to derive useful polymer mechanical properties from these measurements, sandwich structure mechanics[10] was used to determine relationships to connect the bulk material properties to the lumped element values. Specifically, we found

$$E_p = \frac{12}{t^3}\left[\frac{kL^3}{3w} - \frac{E_f t_{Al}^3}{6} - \frac{E_f t_{Al}(2t_{Al}+t)^2}{2}\right] \quad (1)$$

and

$$\rho_p = \frac{1}{t}\left[\left(\frac{E_f t_{Al}^3}{6} + \frac{E_p t^3}{12} + \frac{E_f t_{Al}(2t_{Al}+t)^2}{2}\right) * \left(\frac{2\pi f_p L^2}{n^2}\right)^{-2} - 2\rho_f t_{Al}\right] \quad (2)$$

where E_p is the polymer modulus, t is the thickness of the polymeric section of the cantilever, L is the length of the probe, w is the width of the probe, E_f is the modulus of the aluminum film (including a 3 ± 0.25 nm aluminum oxide layer that forms upon exposure to air),[11] t_{Al} is the thickness of the aluminum films, ρ_p is the polymer density, n is the integration constant for the principal mode (n = 1.87),[12] and ρ_f is the density of the aluminum film (again, considering the oxide layer). Such analysis allows the computation of polymer properties as a function of the two-photon optical dosage D calculated as

$$D = \frac{l(Pp)^2}{v} \quad (3)$$

where P is the measured average laser power, p is the fractional power setting at 1.0 power scaling, l is the length of the path along which the laser is moved when writing each probe (taking into account the slicing and hatching), and v is the scan speed

of the laser spot.[13] Due to the specialized printing process (high level of overlap), the power settings used were unconventional, and so a map of D versus writing parameters v and p is plotted to identify the specific combinations that were studied (Figure 2d). At $D < 7$ W^2 ms, there was insufficient crosslinking resulting in an unusably soft probe. When $D > 30$ W^2 ms, gas bubbles were observed to nucleate during the printing process, and due to the difference in refractive index between the voids and the resin, resultant probes were highly distorted.[14]

Studying the mechanics of probes produced by DLW lithography allowed us to explore the two-photon dosage-dependent properties of photoresist in a manner that may impact researchers beyond those interested in implementing 3D printed MEMS devices. Caution is warranted, however, in assigning material properties based upon design dimensions as the geometry of the final structure was found to change slightly in a D-dependent manner because the volume of the voxel increases with increasing D.[15] To account for this, the geometric parameters were adjusted to reflect the true size of the probe (Figure S2, Supporting Information) as measured by scanning electron microscopy (SEM). With these true geometric parameters in hand, we determined the relationship between D and material properties, showing that both E_p and ρ_p were strongly influenced by D and not by either p or v alone (Figure 2e,f). E_p was observed to fall within the range of reported values for IP-dip[16] and stiffen with increased D (Figure 2e), as has previously been explained by an increase in crosslink density with increasing D.[17] In order to evaluate this trend, E_p was fit using the expression $E_P = E_0 [1 - (D_E/D)^2]$, with $D_E = 5.16 \pm 0.50$ W^2 ms and $E_0 = 3.07 \pm 0.12$ GPa found using nonlinear least squares fitting. While ρ_p also fell within the expected range,[18] we found that it increased slightly with increasing D (Figure 2f). This trend is well represented by $\rho_P = \rho_0 [1 - (D_\rho/D)^2]$ with $D_\rho = 3.23 \pm 0.84$ W^2 ms and $\rho_0 = 1.01 \pm .04$ g cm^{-3}. This observation suggests that probes printed using $D < 10$ W^2 ms are not fully crosslinked, possibly allowing some uncrosslinked polymer to escape during the postprinting rinse. A potential concern when employing polymers is that they may absorb moisture or degrade over time. In order to explore whether these phenomena are playing a role in our 3D printed probes, AFM measurements on polymeric probes were repeated 70 d after initial fabrication. Importantly, we found that f_p changed by less than 0.5% and k was consistent within 2%, signifying that stability in atmospheric conditions is not a major concern for these probes.

Having shown that 3D printed AFM probes can attain lumped element properties commensurate with those of conventional AFM probes, we sought to explore whether they could effectively image surface topography. Initially, we studied the ability of 3D printed probes to image in contact mode as this is a conceptually simpler process than intermittent or noncontact modes. In a typical contact-mode imaging experiment, a probe was mounted in the AFM system and calibrated. Here, a probe with $k = 10.3$ N m^{-1} and $f_p = 122.5$ kHz was used. In order to obtain the highest possible resolution images, a conical tip was 3D printed at the end of the cantilever with a 63× magnification objective. In this case, the probe was found by SEM to have a terminal tip radius of 200 nm (**Figure 3**a). While this sharpness is below what is commonly used for high resolution imaging, it is on par with probes used for nanomechanical characterization[19] or studying soft materials.[20] Further, it is important to note that methods exist for sharpening polymer cones including pyrolysis.[7,21] However, for the purposes of validating that 3D printed probes can image, small tip radii are not necessary as vertical resolution is invariant of probe radius for surface structures larger than the tip radius. Initially, topographic images were generated of a calibration grid sample (Figure 3b) showing that true determination of surface topography is possible with 3D printed probes. Here, imaging was performed at 31.2 µm s^{-1} with a deflection set point of 0.8 V. In addition, prolonged imaging (more than eight hours) was observed with little change in image quality (Figure 3c). Importantly, imaging fidelity was verified through comparison with SEM and images of the same substrate generated using a conventional silicon probe (Figure S3, Supporting Information).

Contact mode imaging, despite being simple, is less common than other more complex modes. In fact, the low Q exhibited by polymeric probes potentially signifies that their bandwidth in intermittent-contact amplitude modulation (AM) AFM imaging can proceed nearly an order of magnitude faster than with conventional silicon probes.[22] Specifically, the bandwidth in an AM-AFM measurement, or the rate at which information can be extracted from the surface, is given by f_p/Q. Simply put, the higher the Q of a given resonator, the longer the energy from a given interaction persists. A major effort inside the AFM community has been focusing on speeding up the imaging process[23] and reducing Q has been identified as a promising route to accomplishing this.[24] In order to explore the potential of 3D printed AFM probes to be useful for high speed imaging, we printed and mounted a probe selected to have f_p and k commensurate with a conventional AM-AFM probe. Importantly,

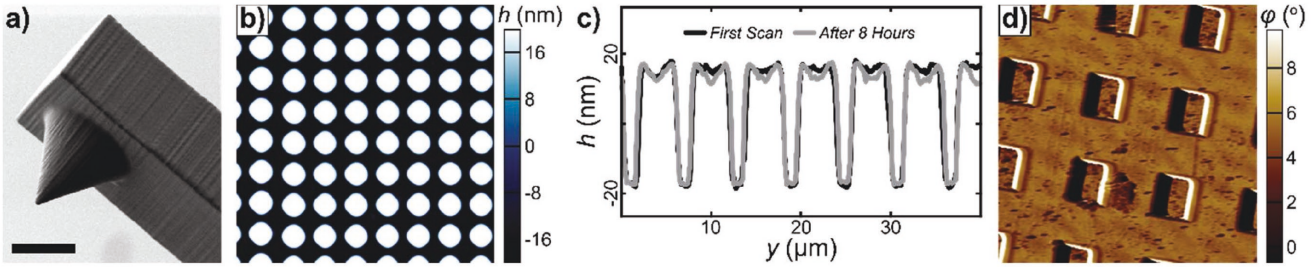

Figure 3. a) SEM of a 3D printed AFM probe. Scale bar is 25 µm. b) AFM height h map of a 40 nm tall calibration sample with taken with a 3D printed probe in contact mode, scan size is 50 µm. c) Profile of h versus positon y showing the first scan and a scan taken after 8 h of continuous imaging. d) Ultrafast AFM phase map of calibration grating taken with a 3D printed probe in intermittent contact mode scanning at 26 Hz, scan size is 30 µm.

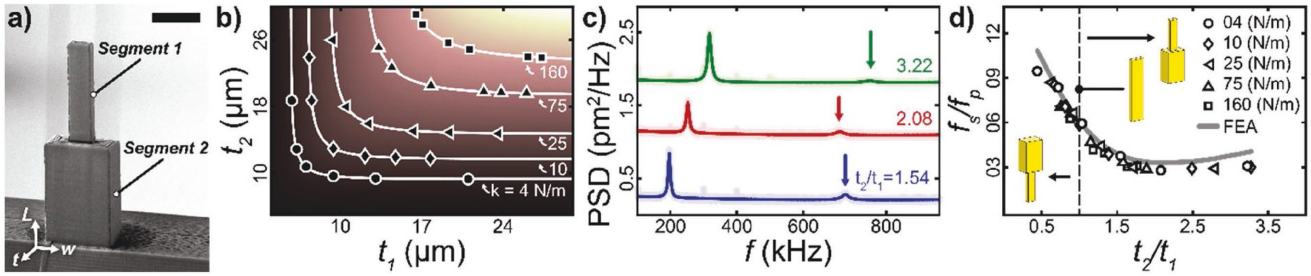

Figure 4. a) SEM of bisegmented 3D printed AFM probes where each segment has a defined thickness t, width w, and length L. Scale bar is 30 μm. b) Map of stiffness k versus segment thicknesses t_1 and t_2 computed using Equation (4). Contours of constant k are shown with points indicating the structures that were studied. c) AFM measured thermal PSD versus f for different segment ratio probes. Arrows indicating the second vibrational resonance. Spectra are vertically shifted for clarity. Dark lines denoting a running average are overlaid on lighter lines that represent the unprocessed data. d) Ratio between the second and principal vibrational resonance frequency f_s/f_p versus segment ratio t_2/t_1. Despite varying in k over a factor of 40, all data collapse onto one curve which agrees with finite element analysis shown as a gray line. Uncertainty in AFM measurements is smaller than the data points.

the 3D printed probe exhibited $Q = 21$, which is a factor of ten smaller than conventional probes with similar geometries. Once printed, assembled, and characterized, we mounted the 3D printed probe in a high speed AFM [Oxford Instruments—Cypher S] and imaged a test sample at high speed (Figure 3d). Not only could the probe readily generate an image at this high speed, but the image quality exhibited no degradation throughout 200 repeated scans at 26 Hz. In these experiments, scan speed was 1.56 mm s^{-1} for a 30×30 μm^2 image.

In addition to the first harmonic mode which is most commonly used for AM-AFM, the higher harmonics of probes are widely used for other imaging modalities.[25] In order to explore the ability of 3D printing to enable access to higher order harmonics, we performed a series of coupled experiments and finite element simulations studying the harmonic modes of bisegmented probes. Specifically, we studied rectangular probes wherein the probe was divided in half with the half attached to the support having a thickness t_2 and the free half having a thickness t_1 (**Figure 4**a). For ease of analysis, the lengths of each segment were kept the same $L_1 = L_2$ and the widths of each segment were set to be double their thickness, and groups of probes with similar k values were determined using the relation

$$k = \frac{3E_p}{L^3}\left(\frac{42}{t_2^4} + \frac{6}{t_1^4}\right)^{-1} \quad (4)$$

Figure 4b shows a map of predicted k, with iso-stiffness lines at a range of relevant k has been drawn with points indicating the combinations that were experimentally explored.

Initially, we performed finite element simulations of these probes using COMSOL Multiphysics. In particular, we found that while the magnitude of f_1 and f_2 were determined by both t_1 and t_2, the ratio f_2/f_1 is exclusively dependent on t_2/t_1 (Figure 4d) and that the change in geometry was able to push f_2/f_1 well above and below the characteristic ratio for a single segmented cantilever. The relationship between the third and first harmonic indicates a similar t_2/t_1-dependent trend (Figure S4, Supporting Information). In order to test these predictions experimentally, we 3D printed a series of bisegmented probes and measured the location of their first and second resonances using a commercial AFM (Figure 4c). The first two peaks can be found robustly using active tuning and, depending on k, by examining the thermal power spectrum. Importantly, good agreement is found between the simulated ratio and the experimentally determined ratio (Figure 4d). This is an important result for two reasons, (1) the good agreement between experiment and theory means that more complex non-rectilinear probes can be explored in simulation prior to printing and (2) the fact that f_2/f_1 can be tuned to exactly 3 (at $t_2/t_1 = 3.27$) indicates that resonantly enhancing nonlinear tip–sample interactions could be possible, opening new possibilities for imaging.

In summary, we have explored whether 3D printed structures can function as AFM probes and found that not only can 3D printed probes be used for imaging, but that they introduce novel capabilities that have the potential to advance the field of AFM. Specifically, the low Q of polymer probes allows them to scan with an order of magnitude higher bandwidth than conventional probes. In addition to this benefit, being able to print probes in an entirely on-demand fashion could accelerate the pace of AFM research. Further, the freedom to design entirely new types of probes could allow researchers to pursue new types of tip–sample interactions such as programmably nonlinear force distance curves that allow soft samples to be robustly imaged[26] or tailoring the mass of the probe to facilitate inertial sensing.[27] Finally, the implications of this work extend beyond AFM as these studies allowed us to explore processing-dependent material properties of polymer written by DLW. Combining the implications for AFM probe design and insights into printed materials, this work provides a compelling example of how additive manufacturing techniques could augment state-of-the-art conventional micromachining.

Supporting Information

Supporting Information is available from the Wiley Online Library or from the author.

Acknowledgements

This work was supported by the Air Force Office of Scientific Research (Multidisciplinary University Research Initiatives FA9550-16-1-0150). N.A. acknowledges support from a BUnano Cross-Disciplinary Fellowship. K.A.B. acknowledges support from the Gordon and Betty Moore Foundation. A.E.W. and C.L. acknowledge support from the

Boston University Photonics Center. The authors acknowledge helpful discussion from Rachael K. Jayne.

Conflict of Interest

The authors declare no conflict of interest.

Keywords

additive manufacturing, atomic force microscopy, direct laser writing, two-photon polymerization

Received: January 12, 2018
Revised: February 23, 2018
Published online: March 30, 2018

[1] a) J. W. Judy, *Smart Mater. Struct.* **2001**, *10*, 1115; b) N. Maluf, K. Williams, *Introduction to Microelectromechanical Systems Engineering*.Artech House, Norwood, USA **2004**.
[2] F. J. Giessibl, *Rev. Mod. Phys.* **2003**, *75*, 949.
[3] E. Snow, P. Campbell, *Appl. Phys. Lett.* **1994**, *64*, 1932.
[4] a) M. Vaezi, H. Seitz, S. Yang, *Int. J. Adv. Manuf. Technol.* **2013**, *67*, 1721; b) C. A. Lissandrello, W. F. Gillis, J. Shen, B. W. Pearre, F. Vitale, M. Pasquali, B. J. Holinski, D. J. Chew, A. E. White, T. J. Gardner, *J. Neural Eng.* **2017**, *14*, 036006.
[5] a) T. Tanaka, H.-B. Sun, S. Kawata, *Appl. Phys. Lett.* **2002**, *80*, 312; b) M. Malinauskas, A. Žukauskas, S. Hasegawa, Y. Hayasaki, V. Mizeikis, R. Buividas, S. Juodkazis, *Light: Sci. Appl.* **2016**, *5*, e16133.
[6] a) R. K. Jayne, T. J. Stark, J. B. Reeves, D. J. Bishop, A. E. White, *Adv. Mater. Technol.* **2018**, *3*, 1700293; b) F. Klein, B. Richter, T. Striebel, C. M. Franz, G. V. Freymann, M. Wegener, M. Bastmeyer, *Adv. Mater.* **2011**, *23*, 1341; c) J. K. Hohmann, M. Renner, E. H. Waller, G. Von Freymann, *Adv. Opt. Mater.* **2015**, *3*, 1488.
[7] G. Göring, P.-I. Dietrich, M. Blaicher, S. Sharma, J. G. Korvink, T. Schimmel, C. Koos, H. Hölscher, *Appl. Phys. Lett.* **2016**, *109*, 063101.
[8] R. Kirchner, N. Chidambaram, M. Altana, H. Schift, in *Laser 3D Manufacturing IV*, Vol. *10095*, International Society for Optics and Photonics **2017**, p. 1009507.
[9] J. E. Sader, J. W. M. Chon, P. Mulvaney, *Rev. Sci. Instrum.* **1999**, *70*, 3967.
[10] D. Zenkert, *An Introduction to Sandwich Construction*, Engineering Materials Advisory Services, Warrington, UK **1995**.
[11] a) T. Campbell, R. K. Kalia, A. Nakano, P. Vashishta, S. Ogata, S. Rodgers, *Phys. Rev. Lett.* **1999**, *82*, 4866; b) E. A. Gulbransen, W. Wysong, *J. Phys. Colloid Chem.* **1947**, *51*, 1087.
[12] K. Ekinci, *Small* **2005**, *1*, 786.
[13] a) S. Hengsbach, A. D. Lantada, *Adv. Eng. Mater.* **2015**, *17*, 172; b) L. Jiang, J. Campbell, Y. Lu, T. Bernat, N. Petta, *Fusion Sci. Technol.* **2016**, *70*, 295.
[14] a) T. Baldacchini, *Three-Dimensional Microfabrication Using Two-Photon Polymerization: Fundamentals, Technology, and Applications*, Elsevier, Amsterdam, The Netherlands **2015**; b) C. N. Lafratta, T. Baldacchini, *Micromachines* **2017**, *8*, 101.
[15] a) H.-B. Sun, K. Takada, M.-S. Kim, K.-S. Lee, S. Kawata, *Appl. Phys. Lett.* **2003**, *83*, 1104; b) M. Thiel, J. Fischer, G. Von Freymann, M. Wegener, *Appl. Phys. Lett.* **2010**, *97*, 221102; c) D. Serien, S. Takeuchi, *Appl. Phys. Lett.* **2015**, *107*, 013702.
[16] H. Zeng, P. Wasylczyk, C. Parmeggiani, D. Martella, M. Burresi, D. S. Wiersma, *Adv. Mater.* **2015**, *27*, 3883.
[17] E. D. Lemma, F. Rizzi, T. Dattoma, B. Spagnolo, L. Sileo, A. Qualtieri, M. De Vittorio, F. Pisanello, *IEEE Trans. Nanotechnol.* **2017**, *16*, 23.
[18] a) J. Bauer, S. Hengsbach, I. Tesari, R. Schwaiger, O. Kraft, *Proc. Natl. Acad. Sci. USA* **2014**, *111*, 2453; b) A. Schroer, J. Bauer, R. Schwaiger, O. Kraft, *Extreme Mech. Lett.* **2016**, *8*, 283.
[19] a) L. Li, L. M. Encarnacao, K. A. Brown, *Appl. Phys. Lett.* **2017**, *110*, 043105; b) J. T. Pham, F. Schellenberger, M. Kappl, H.-J. Butt, *Phys. Rev. Mater.* **2017**, *1*, 015602.
[20] a) Q. Li, G. Lee, C. Ong, C. Lim, *Biochem. Biophys. Res. Commun.* **2008**, *374*, 609; b) Z. Huang, L. Li, X. A. Zhang, N. Alsharif, X. Wu, Z. Peng, X. Cheng, P. Wang, K. A. Brown, Y. Wang, *Adv. Mater.* **2017**, *30*, 1705303.
[21] A. Zakhurdaeva, P.-I. Dietrich, H. Hölscher, C. Koos, J. G. Korvink, S. Sharma, *Micromachines* **2017**, *8*, 285.
[22] R. Garcia, R. Perez, *Surf. Sci. Rep.* **2002**, *47*, 197.
[23] a) G. Schitter, K. J. Astrom, B. E. Demartini, P. J. Thurner, K. L. Turner, P. K. Hansma, *IEEE Trans. Control Syst. Technol.* **2007**, *15*, 906; b) T. Ando, T. Uchihashi, N. Kodera, D. Yamamoto, A. Miyagi, M. Taniguchi, H. Yamashita, *–Eur. J. Physiol.* **2008**, *456*, 211.
[24] J. D. Adams, B. W. Erickson, J. Grossenbacher, J. Brugger, A. Nievergelt, G. E. Fantner, *Nat. Nanotechnol.* **2016**, *11*, 147.
[25] a) R. Hillenbrand, M. Stark, R. Guckenberger, *Appl. Phys. Lett.* **2000**, *76*, 3478; b) R. W. Stark, W. M. Heckl, *Rev. Sci. Instrum.* **2003**, *74*, 5111.
[26] S. Lee, S. Howell, A. Raman, R. Reifenberger, *Phys. Rev. B* **2002**, *66*, 115409.
[27] N. Farmakidis, K. A. Brown, *Langmuir* **2017**, *33*, 5173.

